COMPUTER-AIDED CIVIL AND INFRASTRUCTURE ENGINEERING

Computer-Aided Civil and Infrastructure Engineering **28** (2013) 403–419

An Instrumented Vehicle for Efficient and Accurate 3D Mapping of Roads

Francisco-Angel Moreno, Javier Gonzalez-Jimenez* & Jose-Luis Blanco

Department of System Engineering and Automation, University of Málaga, Málaga, Spain

&

Antonio Esteban

South Regional Direction, SACYR S.A.U., Sevilla, Spain

Abstract: *This article describes an electric vehicle equipped with a laser scanner and a highly accurate absolute positioning system aimed at surveying the geometry of roads. The main advantages of the proposed system with respect to conventional topographic procedures are the possibility of achieving a much higher density of surveyed points and its efficiency while keeping almost the same accuracy—a standard deviation of 12 mm of absolute error. The data acquisition process is managed by an on-board computer which, in a synchronized way, deals with laser scanning and readings from three real-time-kinematics-enabled millimeter GPS receivers. The three-dimensional position and orientation of the vehicle (6 degrees of freedom) all along its trajectory is calculated off-line by a custom software and, with that information, the system also obtains the absolute coordinates of the road scanned points. This article also presents a rigorous description regarding the theory behind 3D reconstruction and the calibration process.*

1 INTRODUCTION

Road pavement is continuously exposed to degradation caused by the transit of vehicles (especially heavy trucks), weathering (basically, rain and temperature changes), and, occasionally, minor terrain movements. Although the inspection of the material properties and quality of the asphalt or concrete are key issues within the global maintenance of roads, in this work we only focus on the topographic problem of surveying their 3D geometry. These data can be compared against the original plans, for example, to certify the work specification, and also to detect and localize the existence of flatness defects (potholes and slight subsidences) that could jeopardize driving safety. Such information is crucial for civil engineers to plan repairing tasks and to assess their cost. The conventional method employed by topographers to acquire 3D data of road surfaces consists of manually surveying a grid-like set of points distributed along the road (typically, about 1 m apart). Normally, this is accomplished by a pair of operators: one of them managing a total station, and the other one placing a ranging rod on the specific point they want to measure. Although this procedure produces highly accurate point coordinates, the so-obtained mesh of points is sparse and the process is very time consuming and error-prone due to operator tiredness.

As an improvement of this traditional method, static 3D laser scanners can be employed to survey a surface and roads in particular. These devices are placed at a known position and must be static during the scanning process. The main advantage of these systems is the extremely dense cloud of points they provide. On the other hand, the process of setting up the operation may become cumbersome and time consuming, though still being faster than the traditional method for large road extensions.

In this article we describe a vehicle, called RoadBot, which collects dense and accurate 3D samplings of road surfaces. This system consists of a computerized, electric vehicle which is equipped with a very accurate

*To whom correspondence should be addressed. E-mail: *javiergonzalez@uma.es*.

DOI: 10.1111/mice.12006

6 degrees of freedom (d.o.f.) GPS-based positioning system and a radial range-finder that scans the road transversally. As the vehicle moves along the road it collects locally referenced 3D data of the scanned surface that are subsequently transformed to a fixed, topographic reference frame. This approach makes easier and speeds up the process of surveying a road getting a cloud of points with density halfway between the traditional procedure and the static 3D laser-based method.

Finally, a complete description of the 3D reconstruction theory and the calibration process is also included.

2 RELATED WORK

Given the relevance of road inspection works, several systems have been previously proposed to address this problem. In civil engineering, some works rely on computer vision techniques to detect concrete cracks (Cord and Chambon, 2012; Nishikawa et al., 2012) or both distresses and deformations (Zhang and Elaksher, 2012) in road surfaces. However, the goal of these works is to detect anomalies on the road surface, not to build a dense point cloud.

On the other hand, other works make use of laser scanners as sensors to find deformations in beam-like structures (Lee and Park, 2011; Park et al., 2007) or to build 3D models of more complex objects such as building facades (Zalama et al., 2011) or civil structures with narrow spaces (Sareen et al., 2012). Furthermore, one of the most widely employed approaches in road surface inspection consists of the usage of a 3D laser scanner which samples the road surface from a fixed position with a 2D field of view (see, for example, Slob and Hack, 2004). Although yielding highly accurate results, these systems are considerably slow as the laser scanner has to be manually placed every few meters. In Li et al. (2010), a system composed of a laser emitter and a camera, both mounted on a vehicle, is proposed to detect pavement distortions. The reported errors in depth and width of rutting and shoving zones fall below 1 cm, though, no global coordinates are provided for the measured points, thus no 3D mapping is performed.

More recently, the company Topcon has released IP-S2 (Topcon, 2012a), a set of commercial systems aimed to map 3D features with a high level of accuracy. In its top-level version, it combines a GPS receiver, an inertial measurement unit and a set of encoders (which provides odometry information) to obtain the full pose (i.e., the position x, y, z, and orientation *yaw*, *pitch*, and *roll*) of the vehicle, although the road is measured by means of a 3D Velodyne laser scanner. Under optimal conditions, the system is reported to achieve a root mean square error in the vehicle pose between 1.5 cm and 5.5 cm for the horizontal plane and between 2 and 3 cm in height. As will be presented here, our system RoadBot outperforms this accuracy in the estimation of the vehicle pose.

The approaches presented in Yu et al. (2007), Ishikawa et al. (2006), Jaakkola et al. (2008), Shi et al. (2008), Kukko et al. (2007), Elberink (2010), Gräfe (2008), and Abuhadrous et al. (2004) are also close to our work as they employ a radial laser scanner to measure the road surface. Among them, a remarkable one because of its performance and similarity to our work is the Mobile-Road-Mapping-System (MoSES) (Gräfe, 2008) developed by the company 3D Mapping Solutions (3D-mapping, 2012), which, as we do here, claims a kinematic survey of roads using laser scanners, in their case mounted on a van. The major advantage of our instrumented vehicle RoadBot in comparison to MoSES is the accuracy in the vehicle pose achieved by the former. RoadBot entirely relies on highly accurate GPS receivers to compute the vehicle position and orientation, two of them with millimeter-accuracy (developed by the company Topcon) and a third one based on RTK (real-time-kinematics) corrections. On the contrary, MoSES uses differential GPS (DGPS) in combination with inertial sensor readings that are integrated over time and, in the long term, reduce the inaccuracies of the positioning measurements. However, due to the high error that DGPS commits in global localization (from some centimeters to tens of meters), there does not exist any guarantee that the estimated vehicle pose is accurate enough from the beginning of the data recording. In contrast, our three-GPS solution allows an immediate, accurate and high-rate direct calculation of the absolute vehicle pose without filtering or approximate estimations. Also, MoSES's output is a digital road model, generated from the set of scanned points, which is subject to the estimation of the model parameters. This may prevent the system to notice highly abrupt irregularities. Opposed to it, RoadBot does not assume any model of the road and just outputs either the raw data or a regular grid with the real measurements, thus detecting any kind of anomalies the road may present.

To assure the claimed accuracy of the surveyed points, it is required to precisely calibrate the GPS devices, the geometric relative position and orientation of the laser scanner with respect to the former, as well as to synchronize all the different data streams from the devices. These issues are addressed in detail in the article.

3 OVERVIEW OF THE ROADBOT SYSTEM

3.1 The vehicle

The system, shown in Figure 1, has been built upon a commercial Yamaha G22 electric buggy that has been

Fig. 1. The vehicle with the sensors and monitoring and control units.

mechanically adapted to host all the electronic and computational devices. The choice of an electric vehicle for this project complies with the reduction of the vehicle's vibrations, the commitment for a respectful behavior toward the natural environment, and the ease of controlling its speed. In this respect, a hand controller that bypasses the vehicle accelerator has been placed next to the steering wheel to offer the optional capability of setting a constant vehicle speed without the need of employing the accelerator pedal. For achieving the desired accuracy in the measurements, RoadBot is designed to operate at a reduced speed, about 3 to 5 km/h.

Moreover, a touch-screen and a keypad have been attached to the dashboard to provide the operator with an easy control and monitoring of the system. The original vehicle batteries provide up to 5 hours of autonomous drive. Our complete set of electronic systems (including sensors, the computer, and the rest of devices) is powered by an additional pack of eight 12V/8 Ah batteries in a combined serial/parallel configuration to build a 24V/32 Ah battery set, which approximately equals the vehicle autonomy. With a full charge of batteries, RoadBot would be able to survey a surface of approximately 20–25 km at a normal operation speed of 5 km/h, hence minimizing the time that traffic must be closed for survey operations. The batteries, together with power converters, fuses, an on-board computer, and all the needed circuitry are all placed within a 19U standard rack at the load zone of the buggy.

A video has been uploaded (UMA, 2011) where the reader can find a more detailed description of the RoadBot vehicle and its operating procedure. The video shows a version of the vehicle previous to the one presented here.

3.2 The sensory and positioning system

The vehicle comprises an outdoor SICK LMS221-30106 (SICK, 2010) radial laser scanner and a set of three TOPCON GPS receivers.

The laser scanner is placed at the rear top part of the vehicle pointing perpendicularly downward, facing the road. It is mounted at a height of approximately 2 m from the ground and programmed to scan at a rate of 37.5 Hz. The angular resolution has been set to 0.5° and the field-of-view is 180°, although it can be reduced by software. According to the manufacturer, its distance resolution is 1 mm although its range error is 10 mm.

The three GPS antennas (whose characteristics are addressed in Section 4) are placed at the uppermost part of the vehicle, whereas a 640×480 video camera has been placed at the rear of the vehicle to record the scanned surface.

3.3 Management and computational system

A Core 2 Duo laptop placed in the rear rack controls the system operation by running a specifically designed Linux-based multi-threaded application, named RoadBotGUI, which will be described in Section 7.1. It performs the configuration of the GPS receivers and the sensors as well as the synchronized recording of the data, including video from the camera.

The position readings from the three GPS receivers are processed to yield a real-time estimation of the vehicle pose with respect to a topographic reference system. This estimated pose is combined with the points measured by the laser scanner to build an on-line, approximate, 3D representation of the road surface.

4 REAL-TIME VEHICLE POSE COMPUTATION

RoadBot combines two different positioning technologies: RTK and millimeter GPS (mmGPS), being the former an improvement of the standard GPS technique and the latter an extension that further refines RTK estimates.

In short, RTK technology improves positioning accuracy by employing carrier phase measurements of

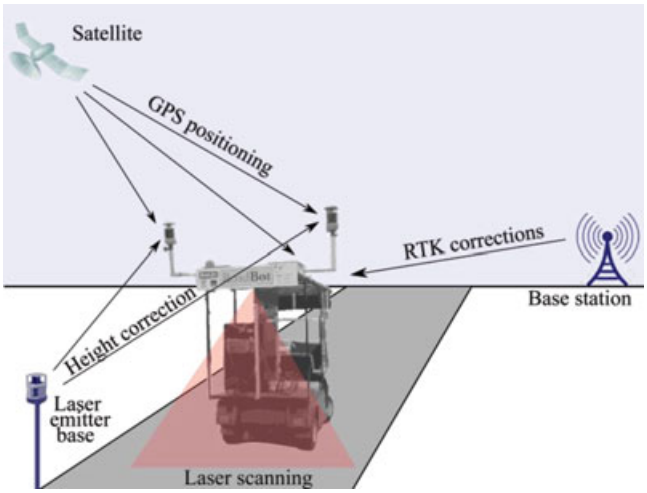

Fig. 2. Scheme of the RTK and mmGPS operation system.

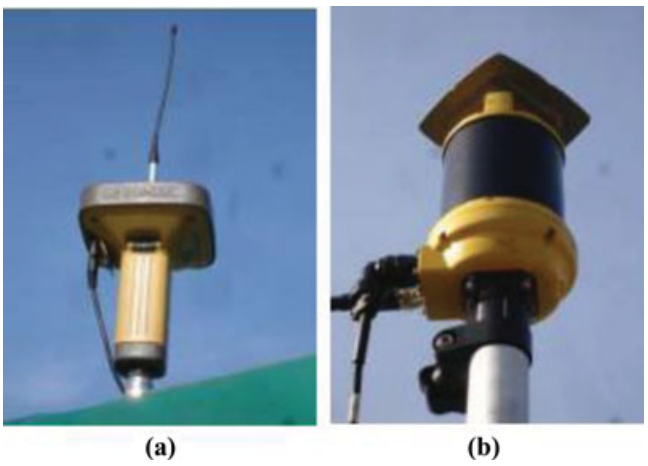

Fig. 3. The GPS receivers used in our application. (a) Topcon RTK-GPS GR-3 and (b) Topcon mmGPS.

GPS signals with real-time corrections provided, via either radio or general packet radio service (GPRS), by a nearby reference station, achieving a typical accuracy up to ±3 cm. This can be meaningfully improved by using the mmGPS technology (refer to Figure 2), developed by the company Topcon, which consists of correcting the RTK-estimated height through a stationary laser transmitter base whose static position has been accurately estimated beforehand (i.e., following a standard topographic method with a total station). A single transmitter emits a signal suitable for working within a range of about 600 meters. Through these station-based corrections the system can achieve a documented accuracy up to ±6 mm in height, becoming the most accurate technology at present for global positioning.

In RoadBot, the front receiver is a Topcon GR-3 (Topcon, 2012b) RTK-GPS, whereas the two rear ones are mmGPS (Topcon, 2012c) (refer to Figures 3a and b, respectively), the latter composed of a dual frequency RTK-GPS antenna and a laser receiver each. The three GPSs send timestamped positioning measurements to the on-board computer at a rate of up to 10 Hz through an RS-232 link. The reason why we employ only two mmGPSs instead of three is that only packs with a maximum of two devices are commercially available. However, to refine the front GPS measurements, we correct its RTK height (at each time step) with the average millimetric correction obtained by the two mmGPS antennas.

4.1 Reference system of the vehicle

The pose of the vehicle is computed by measuring the 3D coordinates (x, y, z) of each GPS antenna and then defining a local coordinate system with origin at the centroid of the two mmGPS positions and the Y-axis pointing toward the left one (refer to Figure 4). The X-axis is computed as a vector perpendicular to the Y-axis, lying on the plane defined by the three GPSs, and pointing forward from the vehicle. Hence the Z-axis, computed as the cross product of the X and Y axes, is pointing upward (almost vertically).

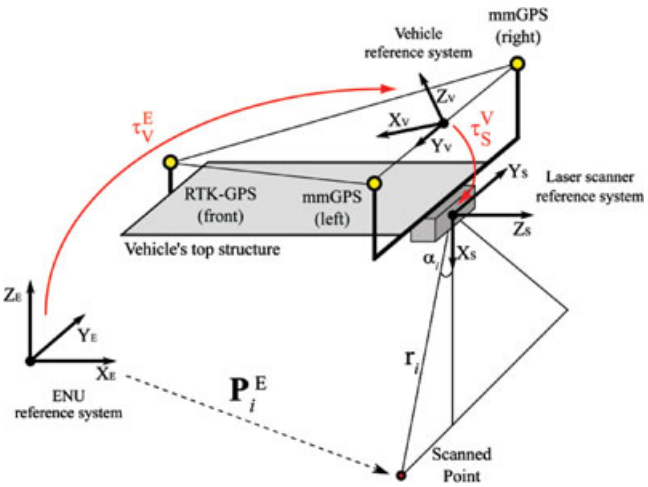

Fig. 4. A schematic representation of the main sensors' positions and the vehicle, laser scanner, and local East-North-Up (ENU) reference system.

Following a common practice in topography, for the sake of minimizing numeric round-off problems it becomes convenient to reconstruct the 3D scanned points in a system of local coordinates whose origin is placed close to the working area. Next we explain the coordinate transformations and the other operations required to achieve this.

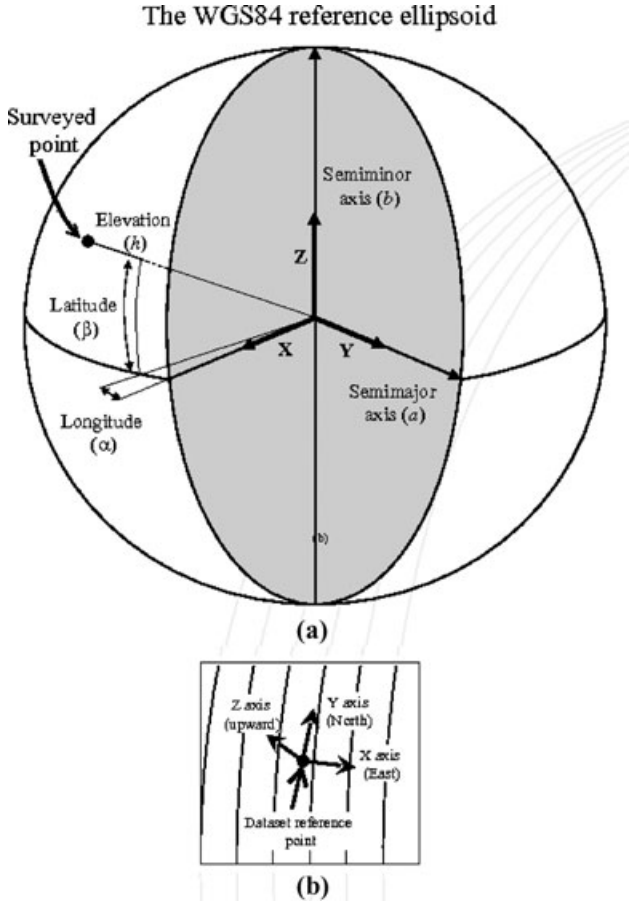

Fig. 5. A schematic representation of the variables involved in the WGS84 reference ellipsoid used for GPS localization. We define a more convenient local Cartesian coordinate system with the origin at an arbitrary location, as shown in (b).

We start with the received GPS coordinates, that is, *longitude*, *latitude*, and *elevation*, which in most receivers are given for the World Geodetic System reference ellipsoid (WGS-84) (NIMA, 2000). That model (see Figure 5a) is optimized such as its center coincides with the center of mass of the Earth as accurately as possible.

Let $\mathbf{D}_i$ be the coordinates of the i-th GPS readings, comprised of longitude α_i, latitude β_i, and elevation h_i, that is, $\mathbf{D}_i = [\alpha_i, \beta_i, h_i]^T$. Then, the geocentric Cartesian coordinates of this point, $\mathbf{G}_i$, can be obtained through (Featherstone and Claessens, 2008):

$$\mathbf{G}_i = \begin{bmatrix} x_i \\ y_i \\ z_i \end{bmatrix} = \begin{bmatrix} (N_i + h_i)\cos\beta_i \cos\alpha_i \\ (N_i + h_i)\cos\beta_i \sin\alpha_i \\ (N_i(\cos\varepsilon)^2 + h_i)\sin\beta_i \end{bmatrix} \quad (1)$$

where the radius of curvature N_i is computed from the latitude, the semi-major axis a, and the angular eccentricity e of the geoid as:

$$N_i = \frac{a}{\sqrt{1 - (\sin e)^2 (\sin \beta_i)^2}} \quad (2)$$

The so-obtained coordinates are, however, of little practical utility given that they are relative to a coordinate system that rotates fixed to the Earth (i.e., the XYZ axes do not have any particular relationship with the working place) and their numerical values are very high (i.e., the origin is the center of the Earth) which is problematic because they then become prone to numeric round-off errors. Hence, it is desirable to transform such coordinates to a known topographic base in the environment whose axes have a more convenient orientation, that is, XY plane being the horizontal and Z pointing upward. This kind of reference system (refer to Figure 5b) is denoted ENU (East-North-Up) and is commonly used in surveying. The change of coordinates are carried out by mapping the geocentric Cartesian 3D points ($\mathbf{G}_i$) into local ENU coordinates ($\mathbf{L}_i$) relative to another point ($\mathbf{R}$) with rotation represented by the three new orthogonal base vectors $\mathbf{u}$ (East), $\mathbf{v}$ (North), and $\mathbf{w}$ (Up). Mathematically, this operation can be written down using homogeneous matrices as:

$$\hat{\mathbf{L}}_i = \begin{bmatrix} \mathbf{u} & \mathbf{v} & \mathbf{w} & \mathbf{R} \\ 0 & 0 & 0 & 1 \end{bmatrix}^{-1} \cdot \hat{\mathbf{G}}_i = \begin{bmatrix} \mathbf{u}^T & -\mathbf{u}^T\mathbf{R} \\ \mathbf{v}^T & -\mathbf{v}^T\mathbf{R} \\ \mathbf{w}^T & -\mathbf{w}^T\mathbf{R} \\ \mathbf{0}_{3\times1} & 1 \end{bmatrix} \cdot \hat{\mathbf{G}}_i \quad (3)$$

where $\mathbf{R}$ stands for the origin of the ENU local reference system, which, in our application, is set to the first position of the left mmGPS. The hat symbol ($\hat{}$) on top of some variables in this equation represents the homogenous version of the correspondent vector. It is important to note that this equation suffers from numerical inaccuracies due to the wide dynamic range of the values within the matrix. Thus, we propose the following rearrangement of the transformation:

$$\hat{\mathbf{L}}_i = \begin{bmatrix} \mathbf{u}^T & 0 \\ \mathbf{v}^T & 0 \\ \mathbf{w}^T & 0 \\ \mathbf{0}_{3\times1} & 1 \end{bmatrix} \cdot (\hat{\mathbf{G}}_i - \hat{\mathbf{R}}) \quad (4)$$

Once the GPS readings have been converted into local Cartesian coordinates, the pose of the vehicle (τ_V^E in Figure 4) can be computed by finding the 6 d.o.f. transformation between such ENU local reference system and that of the vehicle. This can be accomplished

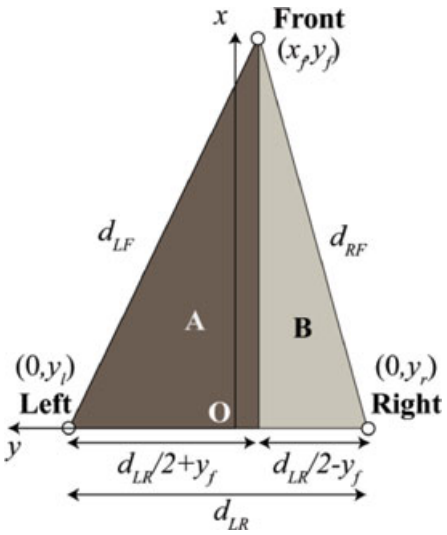

Fig. 6. Positions of the three GPS antennas within the vehicle coordinate system.

from the set of corresponding coordinates of the three GPS receivers in both reference systems by applying the closed-form method published in Horn (1987) and summarized in Appendix B.

4.2 Positions of the GPS receivers

This section addresses the estimation of the three GPS receiver positions with respect to the vehicle reference system. Let $p_f = (x_f, y_f, z_f)$ be the position of the front GPS, and p_l and p_r the analogous for the left and right ones, respectively. As stated before, the vehicle reference system is defined by the positions of the three GPSs, so that they lie on the XY plane. Thus, their Z coordinate in the vehicle reference system is, by definition, zero, thus ($z_f = z_l = z_r = 0$). Moreover, because the Y-axis has been defined on the line that passes through the left and right GPSs, their x coordinates will be also zero ($x_l = x_r = 0$), reducing the problem to computing only the four remaining coordinates: x_f, y_f, y_l, and y_r. This can be performed by using the similar triangles A and B shown in Figure 6, using the following expressions:

$$d_{LF}^2 = x_f^2 + \left(\frac{d_{LR}}{2} + y_f\right)^2$$
$$d_{RF}^2 = x_f^2 + \left(\frac{d_{LR}}{2} - y_f\right)^2 \quad (5)$$

$$d_{LF}^2 - \left(\frac{d_{LR}}{2} + y_f\right)^2 = d_{RF}^2 - \left(\frac{d_{LR}}{2} - y_f\right)^2 \quad (6)$$

which lead to the values of x_f and y_f

$$x_f = \sqrt{d_{LF}^2 - \left(\frac{d_{LR}}{2} - \frac{d_{LF}^2 - d_{RF}^2}{2d_{LR}}\right)^2}$$
$$y_f = \frac{d_{LF}^2 - d_{RF}^2}{2d_{LR}} \quad (7)$$

Finally, the values of y_l and y_r are easily computed from half the distance between the left and right antennas:

$$y_l = \frac{d_{LR}}{2}$$
$$y_r = -\frac{d_{LR}}{2} \quad (8)$$

In Equations (7) and (8), d_{LF}, d_{LR}, and d_{RF} stand for the distances between the left and front, left and right, and right and front GPSs, respectively. These distances are known data, because they can be accurately estimated by collecting a large number of readings from the three receivers (while keeping the vehicle in a static position) and computing the mean distance between their corresponding geocentric coordinates.

The estimated positions of the GPS receivers are shown in Table 1.

5 REAL-TIME VEHICLE POSE COMPUTATION

To achieve the claimed accuracy, it is necessary to estimate the full pose (i.e., both the position (x, y, z) and the orientation (*yaw*, *pitch*, *roll*)) of the laser scanner with respect to the vehicle reference system. Figure 7 can be referred to for an illustration of this procedure.

Here we again employ Horn's method (Horn, 1987) to determine the 6 d.o.f. transformation (τ_S^V) between the laser scanner reference system and that of the vehicle (colored in blue and black in Figure 7a, respectively) using as input the coordinates of nine nonaligned points with respect to both reference systems: $\{\mathbf{P}_i^S\}$ and $\{\mathbf{P}_i^V\}$, respectively, with $i = 1, \ldots, 9$.

For this purpose, we have designed a calibration pattern (shown in Figure 8), composed of a set of three reflective tape targets (of size 4×4 cm) stuck at the top of ranging rods that are fixed at a rigid structure. The coordinates of the center of these reflective tapes will constitute the sets of input points. To get the nine nonaligned points, we manually place the calibration pattern at three different positions (marked #1, #2 and #3 in Figure 7b) while the vehicle remains in a static position.

First, the pattern is placed (about 3 meters away from the vehicle) so that the reflective tapes can be scanned

Table 1
Sensor poses after calibration

Sensor	*x*	*y*	*Z*	*yaw*	*pitch*	*roll*
Laser scanner	0.134 m	0.211 m	−0.773 m	0.10°	79.84°	−177.31°
Front GPS [GR3]	2.545 m	−0.075 m	0.0	X	X	X
Left GPS [mmGPS1]	0.0	0.973 m	0.0	X	X	X
Right GPS [mmGPS2]	0.0	−0.973 m	0.0	X	X	X

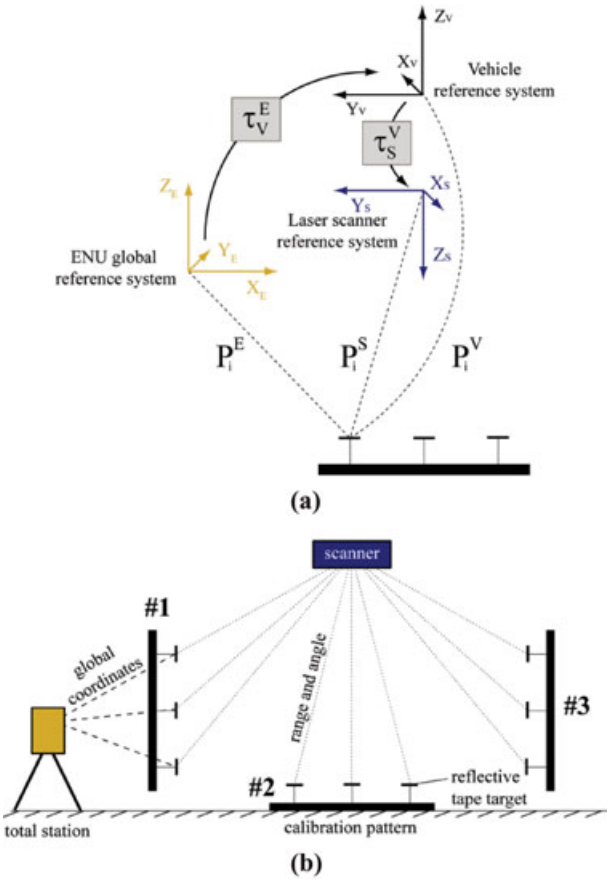

Fig. 7. (a) The involved reference systems in the calibration, the transformation between them and the coordinates of a certain reflective tape target with respect to those systems. (b) The setup for the laser scanner calibration showing the three positions (marked #1, #2, and #3) of the calibration pattern during the procedure.

by the laser sensor (see Figure 7). To overcome the inaccuracies that the angular resolution of the scanner may cause, our software fits a recorded synthetic model of the calibration pattern to the scanner readings with the purpose of estimating the exact range (r_i) and angle (α_i) of the center of the reflective tapes. If the recorded model does not fit the scanned points with a minimum level of accuracy, the calibration is dismissed and the user is asked to repeat the calibration.

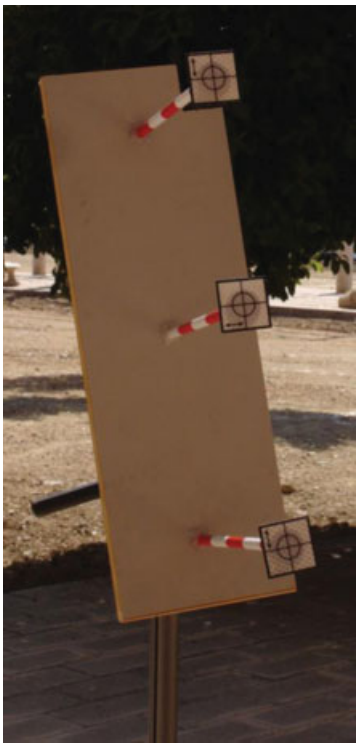

Fig. 8. Pattern for calibrating the laser scanner.

For each position, the procedure performs as follows.

The range and angle values are straightforwardly transformed into coordinates within the laser scanner reference system with:

$$\mathbf{P}_i^{\mathrm{S}} = \left[x_i^{\mathrm{S}}, y_i^{\mathrm{S}}, z_i^{\mathrm{S}}\right]^{\mathrm{T}} = \begin{bmatrix} r_i \cos(\alpha_i) \\ r_i \sin(\alpha_i) \\ 0 \end{bmatrix} \tag{9}$$

yielding this way the first set of coordinates $\{\mathbf{P}_i^{\mathrm{S}}\}$.

On the other hand, and before moving the calibration pattern to the next position, the global coordinates (*latitude*, *longitude*, and *elevation*) of the reflective tapes are measured employing a total station and then transformed to the local ENU reference system through the procedure explained in Section 4, yielding an intermediate set of local points $\{\mathbf{P}_i^{\mathrm{E}}\}$. These local ENU

coordinates are related to the coordinates of the targets with respect to the vehicle reference frame $\{\mathbf{P}_i^{\mathrm{V}}\}$ through the expression:

$$\mathbf{P}_i^{\mathrm{E}} = \tau_{\mathrm{V}}^{\mathrm{E}} \oplus \mathbf{P}_i^{\mathrm{V}} \tag{10}$$

where $\tau_{\mathrm{V}}^{\mathrm{E}}$ stands for the full pose of the vehicle within the ENU reference system, and $\oplus$ represents the pose composition operator. This pose can be estimated again from the GPS measurements as described in Section 4 and it remains constant for the whole calibration procedure, because the vehicle remains static.

Finally, from Equation (10) we can derive $\{\mathbf{P}_i^{\mathrm{V}}\}$ in this way:

$$\mathbf{P}_i^{\mathrm{V}} = \left[x_i^{\mathrm{V}}, y_i^{\mathrm{V}}, z_i^{\mathrm{V}}\right]^{\mathrm{T}} = \left(\ominus\tau_{\mathrm{V}}^{\mathrm{E}}\right) \oplus \mathbf{P}_i^{\mathrm{E}} \tag{11}$$

where $\ominus$ is the inverse pose composition operator.

Thus, we obtain the set of corresponding coordinates $\{\mathbf{P}_i^{\mathrm{V}} \leftrightarrow \mathbf{P}_i^{\mathrm{s}}\}$ needed to estimate the rigid 6 d.o.f. transformation between both reference systems $(\tau_{\mathrm{S}}^{\mathrm{V}})$, hence fully calibrating the laser scanner position within the vehicle reference system.

The numeric results of the laser scanner full pose calibration can be seen in Table 1.

6 3D ROAD RECONSTRUCTION

The 3D reconstruction of the road is performed through the transformation of all the measurements captured with the laser scanner into the local ENU reference system, using the pose transformations indicated in Figure 4, so that $\mathbf{P}_i^{\mathrm{E}} = \tau_{\mathrm{V}}^{\mathrm{E}} \oplus \tau_{\mathrm{S}}^{\mathrm{V}} \oplus \mathbf{P}_i^{\mathrm{V}}$. Each of these transformations has an associated homogeneous matrix (see Equation (14)) which converts the coordinates from one reference system to another.

Formally, let again r_i and α_{i} be the range and angle values, respectively, measured by the laser sensor for a certain scanned point p_i on the road's surface. As stated in the previous section, its coordinates with respect to the laser scanner's reference system $\{\mathbf{P}_i^{\mathrm{S}}\}$ are computed through Equation 9.

Such point can be further transformed with respect to the vehicle reference system $\mathbf{P}_i^{\mathrm{V}}$ with:

$$\mathbf{P}_i^{\mathrm{V}} = \left[x_i^{\mathrm{V}}, y_i^{\mathrm{V}}, z_i^{\mathrm{V}}\right]^{\mathrm{T}} = \mathbf{T}_{\mathbf{S}}^{\mathbf{V}}\mathbf{P}_i^{\mathrm{S}} \tag{12}$$

where $\mathbf{T}_{\mathbf{S}}^{\mathbf{V}}$ is the 4×4 homogeneous transformation matrix associated to the 6 d.o.f. pose change between the laser scanner and the vehicle reference systems $(\tau_{\mathrm{S}}^{\mathrm{V}})$, which is fixed and was previously computed during the calibration process (refer to Section 5).

Finally, the ENU coordinates of the scanned point $\mathbf{P}_i^{\mathrm{E}}$ are computed in a similar way by applying the transformation matrix $\mathbf{T}_{\mathbf{V}}^{\mathbf{E}}$ associated to the vehicle pose within the ENU reference system $(\tau_{\mathrm{V}}^{\mathrm{E}})$ as:

$$\mathbf{P}_i^{\mathrm{E}} = \left[x_i^{\mathrm{E}}, y_i^{\mathrm{E}}, z_i^{\mathrm{E}}\right]^{\mathrm{T}} = \mathbf{T}_{\mathbf{V}}^{\mathbf{E}}\mathbf{P}_i^{\mathrm{V}} \tag{13}$$

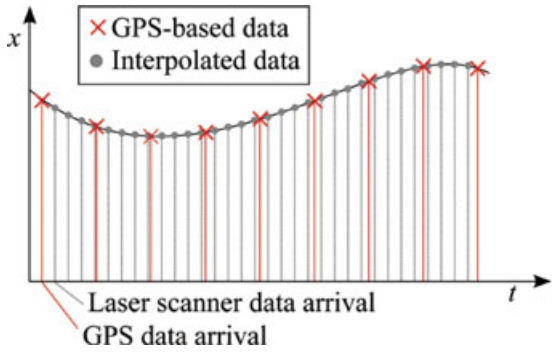

Fig. 9. Schematic representation of the spline interpolation for the x coordinate at the laser data arrival time steps.

The ENU-referenced set of points computed this way constitutes the 3D reconstruction of the road surface.

The homogeneous matrices $\mathbf{T}_{\mathbf{S}}^{\mathbf{V}}$ and $\mathbf{T}_{\mathbf{V}}^{\mathbf{E}}$ associated to the pose transformation between their respective reference systems are computed through this general expression:

$$\mathbf{T} = \begin{pmatrix} CyCp & CySpSr - SyCr & CySpCr + SySr & x \\ SyCp & SySpSr + CyCr & SySpCr - CySr & y \\ -Sp & CpSr & CpCr & z \\ 0 & 0 & 0 & 1 \end{pmatrix} \tag{14}$$

where *Sy*, *Sp*, and *Sr* stand for the sine values of the *yaw*, *pitch*, and *roll* angles (Diebel, 2006), respectively, *Cy*, C*p*, and *Cr* are the analogous symbols for the cosine values, and x, y, and z represent the translation between the involved reference systems.

Note that the transformation between the vehicle and the ENU reference systems (i.e., the vehicle pose within it) $(\tau_{\mathrm{V}}^{\mathrm{E}})$ changes at each time step as the vehicle moves. In our system, the vehicle pose is computed from the GPS measurements at 10 Hz, which is the maximum rate that our GPS devices provide. This means that the system only has a *real* position measurement each 100 ms. However, the scanned points are collected at a rate of 37.5 Hz and, therefore, we need a vehicle pose estimation at that rate to compute the ENU coordinates of all the scanned points in each laser reading. This can be solved by a cubic spline interpolation for all the six elements in the vehicle pose, that is, x, y, z, *yaw*, *pitch*, and *roll*, at the time that the laser data arrive (see Figure 9 for a schematic representation of the x coordinate interpolation).

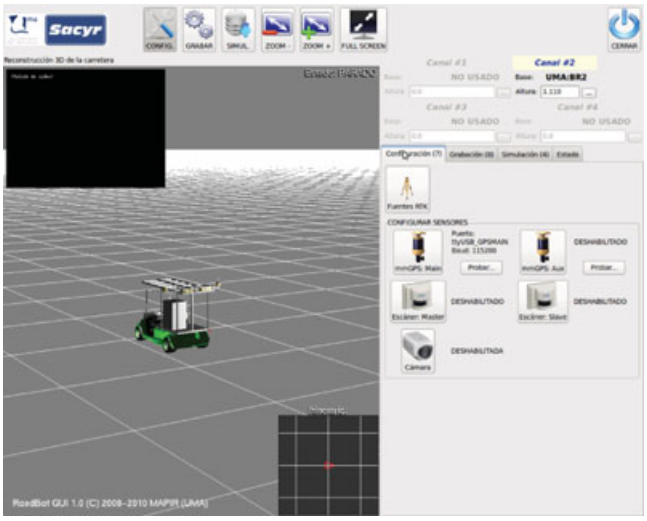

Fig. 10. RoadBotGUI interface.

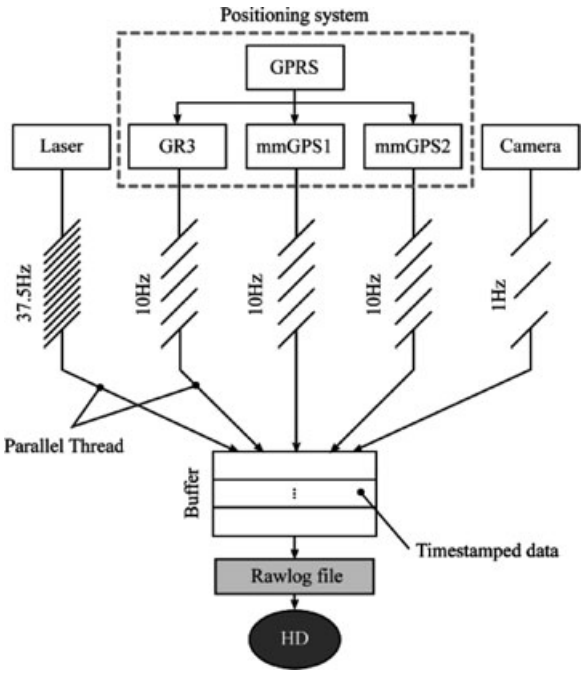

Fig. 11. Threads involved in the data-grabbing process.

Another possibility we tested, and which led to almost identical results, is the application of more advanced rotation interpolation as the widely used SLERP method (Shoemake, 1985).

7 DESCRIPTION OF THE ROADBOT SOFTWARE

This section presents RoadBotGUI and RoabBotStudio, two software applications developed to on-line capture data from the sensors and to off-line process and reconstruct the road surface, respectively.

7.1 RoadBotGUI

RoadBotGUI (see Figure 10) is a multi-threaded application in charge of configuring and synchronizing the vehicle's sensors, as well as recording all the sensory data. This application launches a different thread for each of the sensors and devices included in the grabbing process, that is, the GPS receivers, the laser scanner and the video camera, as it is depicted in Figure 11.

As we mentioned in Section 4, the system can obtain RTK corrections either via radio or by GPRS from a reference station. In the former case both the GR3 and the mmGPS automatically receive and process the incoming corrections and no further work must be done by our software. However, in the latter, RoadBotGUI launches another thread that connects to the reference station (also called NTRIP [Networked Transport of RTCM via Internet Protocol] caster) using a USB GPRS modem to get the real-time corrections. Finally, these data are encapsulated and forwarded to all three GPS receivers through a standard RS232 link.

One of the key issues that must be observed in the data collection process is the correct and precise synchronization of the data from the laser scanner, the camera, and the GPS devices; hence all the grabbed measurements must be appropriately timestamped. Both the GPS readings and the RTK corrections already provide timestamps that are acquired from the satellite clock. However, the rest of the sensors do not provide any timing information and, therefore, RoadBotGUI must generate a timestamp that coherently synchronizes such readings with respect to the *real*, accurate GPS clock. For that purpose we compute the time difference between the timestamp within the GPS readings and the PC local time of their arrival. This difference approximately estimates the delay between both the satellite and the PC clocks, and it is employed to correct the timestamps of the data from the sensors. However, this first estimation does not model possible delays between the laser scanner and the PC, due to buffering and/or transmission times.

To estimate the influence of these other delays, we performed a small experiment where we placed an inclined board on the ground beside the vehicle so that the scanner laser could scan it. Then, from a static position, we started to move forward the vehicle while scanning the board and storing the laser measurements with their associated PC-based timestamps, already

corrected with the first estimation of the delay. Afterward, we detected the time when the laser readings started to decrease (indicating that the laser was scanning up the inclined slope) and when the GPS position started to change (indicating that the vehicle was moving). In this experiment, both times were practically identical, hence validating our first estimation of the delay. The GPS position readings are processed to yield a real-time estimation of the vehicle full pose with respect to the topographic reference system, which, in turn, is combined with the scanned points from the range-finder to build a 3D representation of the road surface, as explained in Section 6. The built surface for the last 5 seconds is shown in real time by the RoadBotGUI interface, to visually check the scanning process. This software application can be easily managed by the user through the on-board touch-screen.

All the grabbed data (except the images) are stored in a single Rawlog file (MRPT, 2012) to be subsequently processed by the RoadBotStudio application, which is described next.

Although RoadBot has been conceived to survey a road with the highest level of accuracy, sometimes it can be interesting to have a 3D representation of a road without such accuracy requirements. In this case, millimetric corrections can be dropped and RoadBotGUI will operate only with RTK corrections, avoiding the limitations of the working area that the laser transmitters impose.

7.2 RoadBotStudio

To perform the 3D road reconstruction, we have designed another application, called RoadBotStudio (see Figure 12), which loads the data recorded by RoadBotGUI, processes them, and off-line reconstructs the whole scanned surface. Besides the reconstructed surface, RoadBotStudio shows additional information about the grabbed data such as the timestamped vehicle trajectory, the evolution of the x, y, and z coordinates and the *yaw*, *pitch*, and *roll* angles of the vehicle or the set of grabbed images at their corresponding points of the trajectory.

RoadBotStudio also analyzes the grabbed data looking for inconsistencies, errors, or problems during the recording process, usually due to a degradation of the GPS information, notifying about them to the end user. For example, if there is an abrupt change in the height measurements, or a repetition of the height, RoadBotStudio will place an indicator on the representation of the vehicle trajectory. Moreover, the mmGPS devices provide some warning codes when the operation conditions are not ideal (e.g., the angle between the laser transmitter and the receiver is near to the working limit,

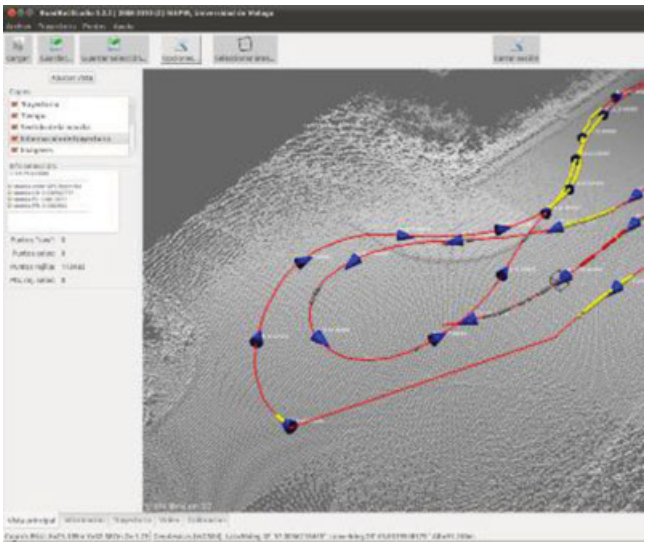

Fig. 12. A snapshot of the RoadBotStudio application.

one of the corners of the laser transmitter is blocking the laser beam, etc.). These situations induce larger errors in the millimetric corrections so, to inform to the final user, those warning codes are also displayed by RoadBotStudio. Further information regarding these issues is presented in Section 9.

Because the number of grabbed points may be considerably high, hence making them difficult to be managed, RoadBotStudio allows the user to filter out undesirable data by selecting either a maximum scanning angle, a certain limit on the road surface, or a height range of the scanned points from the road surface. The user can also load only some parts of the recorded file or either select between showing all the points in the file or to build a regular grid with them. The grid cell's size is configurable whereas the height of the cell is computed as the average height of all the points scanned within it. This last feature allows the user to get a sparser representation of the road, similar to the one built with traditional methods but, thanks to the averaging of the heights, much more accurate.

Finally, RoadBotStudio can export the processed, filtered data to a text file in both the ENU local and the geodetic WGS-84 coordinates for each of the scanned points on the surface, so they can be easily imported into third party commercial software.

8 EXPERIMENTAL RESULTS

This section presents some of the results yielded by the RoadBot system. In all the experiments, the vehicle was driven at a speed of about 4 km/h, achieving a

maximum point cloud density of approximately 12,000 points per navigated meter. Data from the three GPS receivers were recorded at a rate of 10 Hz, with their highest accuracy, that is, the front device in RTK mode, and the rear ones receiving millimetric corrections.

The most time-consuming step in placing the RoadBot in operation is setting up the static laser transmitters because their locations have to be accurately known beforehand. For that, a topographer must survey the base points where the transmitters will be placed. Once this is accomplished, RoadBot is ready to work, because all the sensors are automatically configured at the start-up of the RoadBotGUI application.

As a preliminary validation of the system we survey a road in a parking lot at the campus of the University of Málaga. A top view of the obtained point cloud can be seen in Figure 13a, although some details have been highlighted in Figure 13b. As the top view in Figure 13a shows, the vehicle follows a trajectory with several loops while going up and down along an inclined road, and traversing a parking lot. Figures 14a and b present the x, y, and z coordinates and the *yaw*, *pitch*, and *roll* angles of the vehicle, respectively, during the experiment. Note the smoothness of the position estimation, and the zones where the vehicle navigated downhill and uphill (in the z coordinate plot). On the other hand, the loops that the vehicle performed are clearly visible in the evolution of the *yaw* angle, whereas the other two plots, although presenting a noisy appearance, show spikes in the *pitch* and *roll* angles whose mean values between two consecutive time steps are 0.0002° and -0.00024°, respectively, with standard deviations of 0.11° and 0.12°, respectively.

To check the accuracy of the positioning data provided by the two mmGPS devices, the distance between them, which ideally is constant, has been measured at each time step during the above experiment. The average measured distance between the antennas is 1.944 m although the standard deviation is just 3 mm for a total of more than 7,000 measurements.

In another experiment, we pursued testing the accuracy of the RoadBot system in a more realistic scenario. Concretely, the experimental setup consisted of the navigation of the vehicle through a road (see Figure 15) while simultaneously grabbing data from the laser scanner and with the GPSs operating at their highest accuracy. As before, the vehicle was driven at a speed of about 4 km/h, providing a point cloud with a maximum of about 12,000 points per navigated meter.

The scanned surface was compared afterward to a set of control points distributed on the road (see Figure 16), which were computed as follows: (i) first, the road was scanned by our system RoadBot; (ii) on the other hand,

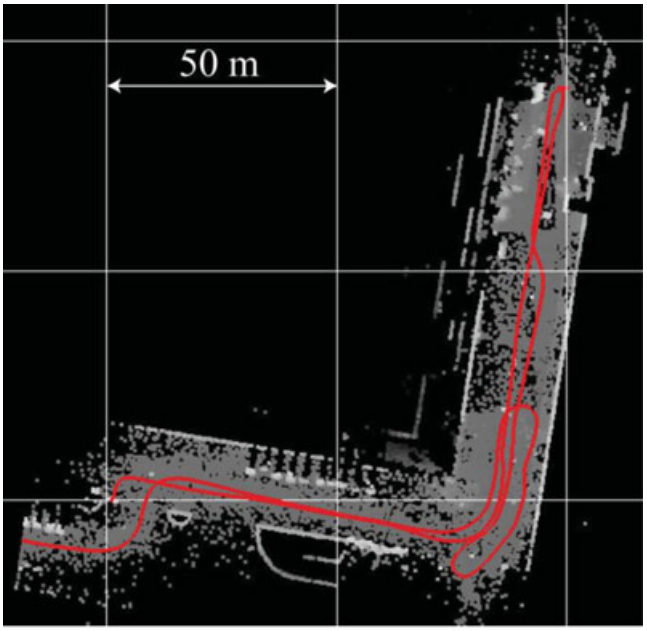

(a)

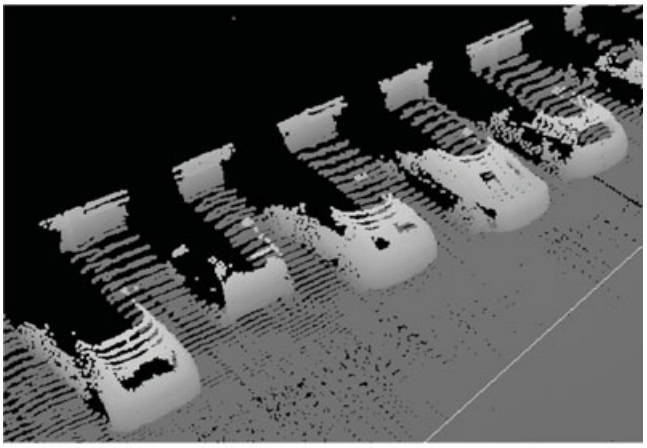

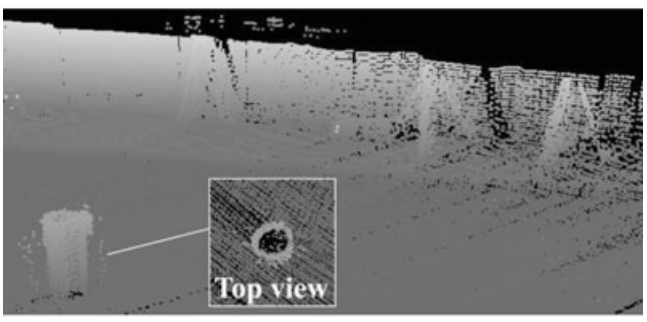

(b)

Fig. 13. (a) A top view of the reconstructed surface at the University of Málaga. The trajectory of the vehicle is plotted in red. (b) (Upper) Some cars in the parking lot, (Lower) reconstructed shapes of a pair of tripods, a ladder, and a barrel. A top view of the barrel is also displayed.

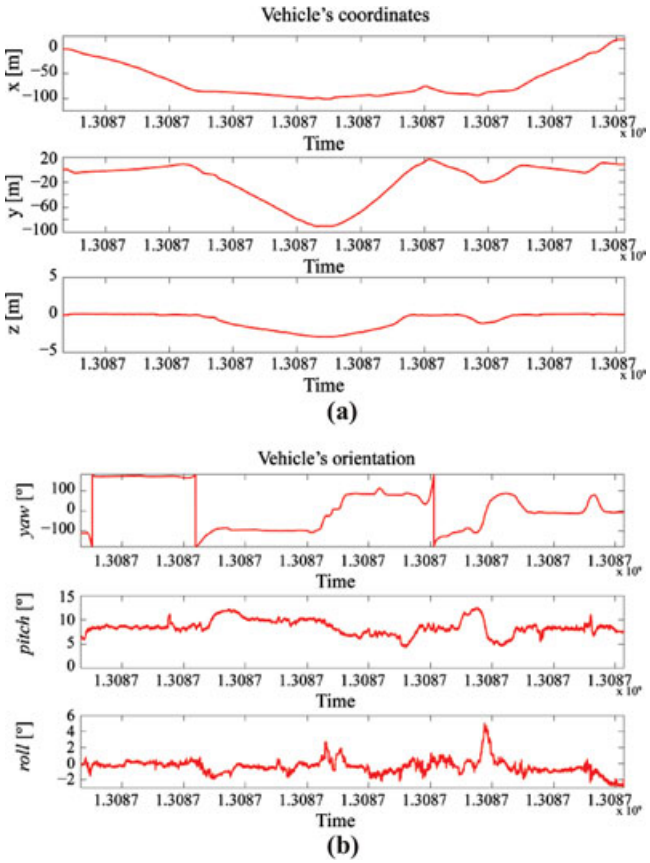

Fig. 14. Evolution of the (a) vehicle's position and (b) orientation during the navigation.

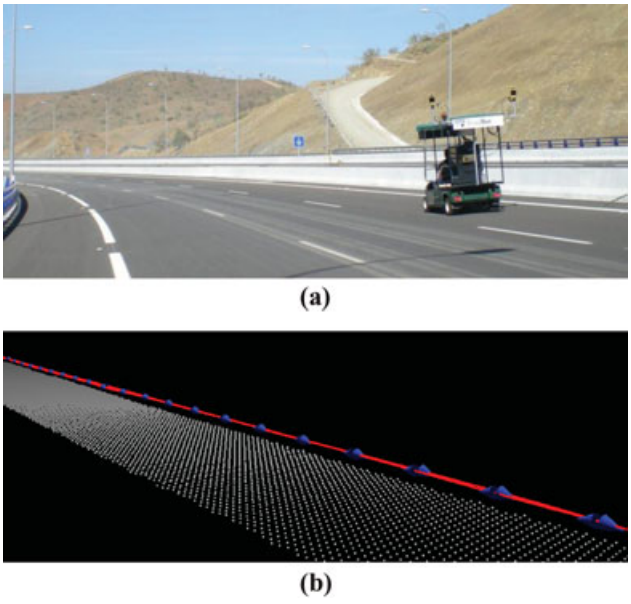

Fig. 15. (a) The RoadBot system operating on a highway during the experiments and (b) the reconstructed surface.

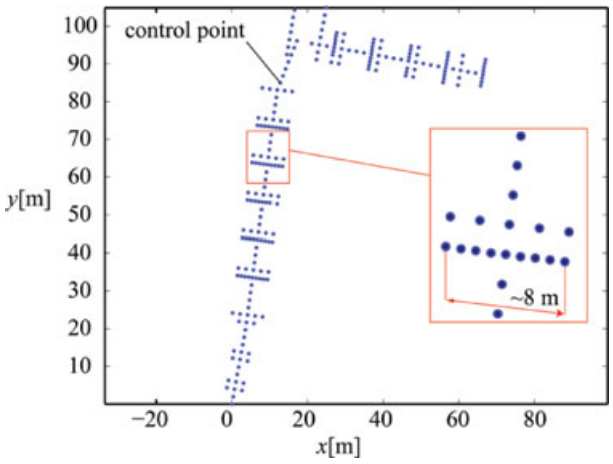

Fig. 16. Distribution of the control points in the experiment.

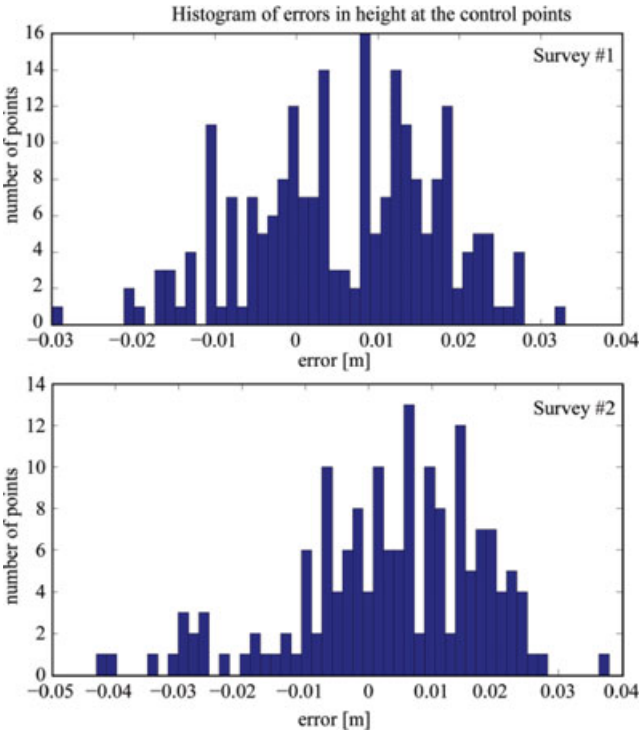

Fig. 17. Histogram of the errors in height at a set of control points.

a topography team manually surveyed a set of more than 200 points (distributed along the road, on a strip of about 8 m width) using a total station so that they were considered our ground truth for the experiment; (iii) finally, the z coordinates in those points were compared against the geometrically closest point within the point cloud, being their distance almost negligible due to its high density. Figure 17 (top) shows the histogram of errors that the system incurs at the control points,

revealing a mean error of 6 mm with a standard deviation of 12 mm. Figure 17 (bottom) shows the similar results for another survey of the same road.

The two main sources of error that affect the system performance are the inaccuracies of the sensors and a miscalibration of the laser scanner. The error in distance of the laser scanner and the error in height of the GPS devices are additively related with the errors in height of the scanned points, affecting more acutely those scanned just under the vehicle (as analytically demonstrated in Appendix A). On the other hand, a miscalibration of the laser scanner (especially regarding its orientation) affects more severely the points scanned with larger angles. A more thorough derivation is presented in Appendix A.

In this experiment, because the width of the scanned strip under the vehicle was limited to 8 m, there were not significant differences in the distribution of the errors at the control points according to their distance to the vehicle. However, the non-zero average error (6 mm) reveals some kind of miscalibration of the laser scanner.

9 LIMITATIONS OF THE ROADBOT SYSTEM

The main limitations of the proposed system are related to the loss of coverage of the GPS, which are (in increasing level of importance): low quality of millimetric corrections, complete loss of the millimetric corrections, loss of the RTK corrections, and loss of the GPS signal. Obviously, all these situations produce a degradation of the final accuracy and, therefore, they must be detected by the post-processing software, to warn the final user about a low performance of the system in those zones.

RoadBot has been designed to work with at least RTK-level accuracy in the estimation of its global position. Thus, a loss of RTK corrections, caused either by interferences in the radio channel or instability of the NTRIP stream, will cause a blank area in the resulting representation of the scanned surface (see Figure 18) until, at least, the RTK corrections are recovered.

On the other hand, millimetric corrections can be lost if the vehicle loses the line of sight with all the laser transmitters. In this case, RoadBotGUI will continue recording data but, offline, RoadBotStudio will mark those zones as "only-RTK" when showing them to the user. Besides, it may happen that only one of the antennas loses line of sight with the transmitter, producing a wrong estimation of the vehicle orientation and, therefore, an undulation in the reconstructed surface (as shown in Figure 19).

Even if the millimetric corrections are not completely lost, there may be a degradation of their quality, for example, when the receiver is being partially occluded by

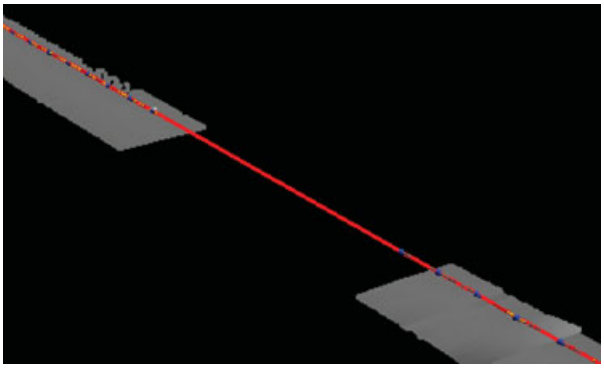

Fig. 18. A gap in the scanned area due to a loss of GPS coverage.

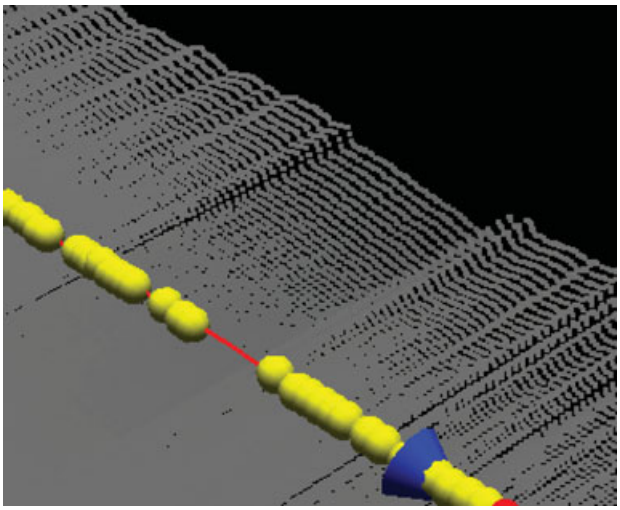

Fig. 19. The undulation produced by an antenna losing the line of sight with the laser transmitter.

one of the corners of the laser transmitter itself, or when the vehicle is close to the limit of the transmitter's working range. This issue is also indicated by RoadBotStudio (shown in Figure 20).

Finally, during the development of the system, we found the system performance to be highly dependent on the GPS receiving rate. Setting up a GPS data rate of 5 Hz produced some inaccuracies in the final reconstructed surface because some of the vehicle movements (e.g., small vibrations when passing on potholes) were not properly captured by the positioning system, hence producing errors in the output scanned point cloud. Working at a GPS data rate of 10 Hz suffices to overcome the problem.

10 FUTURE WORKS AND CONCLUSION

This article has presented an electric vehicle, called RoadBot, equipped with a set of sensors and a computer

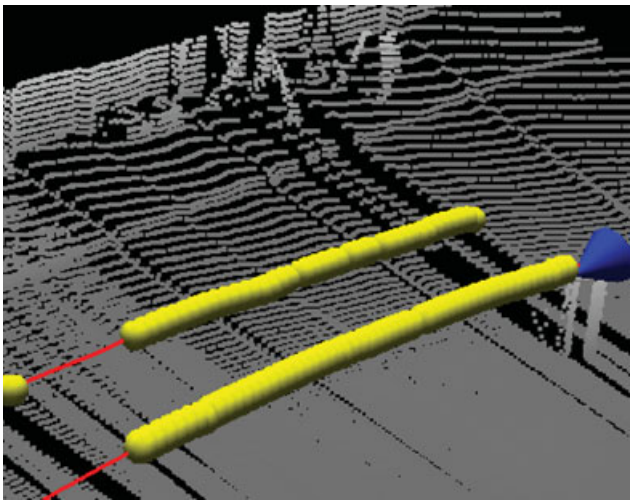

Fig. 20. The yellow indicators on the trajectory that mark the area where the corner of the laser transmitter shades the receptors.

to automate the collection of dense and precise 3D points from a road surface. The system combines highly accurate state-of-the-art GPS technologies to estimate the 6 d.o.f. pose of the vehicle with an outdoor laser range-finder that scans the road surface while the vehicle traverses the road. Two different software applications have been developed: one, so-called RoadBotGUI, which deals with the on-line operation of the vehicle (configuration and synchronization of the devices, GPS positioning, laser scanner measurements, video grabbing, etc.), and another, so-called RoadBotStudio, which deals with data manipulation and visualization, including the 3D reconstruction of the road surface.

In the future, besides road surveying, RoadBot could accomplish different applications such as automatic detection of anomalies (cracks, potholes, etc.) on the road's surface, or traffic signs inventory where the camera could play a more significant role than it plays in the current configuration. In this sense, our system would be able to automatically color the cloud of points, making easier the management of the RoadBot's output by the end user or, also, the images could help to enhance the calibration process by drawing on an image the profile that the laser sensor is scanning.

The results obtained with RoadBot show average errors of about 6 mm at a set of control points with a standard deviation of 12 mm while significantly improving the road inspection procedure with a high increase in both the density of scanned points and the speed of the traditional survey procedure.

The developed prototype is being currently exploited by the topography department of the company SACYR S.A.U. in Spain.

ACKNOWLEDGMENTS

This work has been promoted and supported by the company SACYR S.A.U. under the contract OTRI-8.06/5.56.2922 and partially supported also by the Plan Nacional de Investigación, project DPI08-03527.

REFERENCES

3D-mapping (2012), 3D-mapping solutions webpage. Available at: http://www.3d-mapping.de/, accessed January 5, 2013.

Abuhadrous, I., Ammoun, S., Nashashibi, F., Goulette, F. & Laurgeau, C. (2004), Digitizing and 3D modeling of urban environments and roads using vehicle-borne laser scanner system, in *Intelligent Robots and Systems, 2004 (IROS 2004). Proceedings 2004 IEEE/RSJ International Conference*, vol. 1, 76–81.

Cord, A. & Chambon, S. (2012), Automatic road defect detection by textural pattern recognition based on AdaBoost, *Computer-Aided Civil and Infrastructure Engineering*, **27**, 244–59.

Diebel, J. (2006), *Representing Attitude: Euler Angles, Unit Quaternions, and Rotation Vectors*, Stanford University, CA.

Elberink, S. O. (2010), Acquisition of 3D topography: automated 3D road and building reconstruction using airborne laser scanner data and topographic maps. Ph.D. thesis, International Institute for Geo-information Science and Earth Observation.

Featherstone, W. & Claessens, S. (2008), Closed-form transformation between geodetic and ellipsoidal coordinates, *Studia Geophysica et Geodaetica*, **52**(1), 1–18.

Gräfe, G. (2008), Kinematic 3D laser scanning for road or railway construction surveys, in *Proceedings of the International Conference on Machine Control & Guidance*, Zurich, Switzerland, June 24–26, 2008.

Horn, B. (1987), Closed-form solution of absolute orientation using unit quaternions, *Journal of the Optical Society of America A*, **4**(4), 629–42.

Ishikawa, K., Onishi, T., Amano, Y., Hashizume, T., Takiguchi, J., Fujishima, T. & Tanaka, Y. (2006), Development of a vehicle-mounted road surface 3D measurement system, *Proceedings of 23rd International Symposium on Automation and Robotics in Construction*, Tokyo, Japan, October 3–5, 2006.

Jaakkola, A., Hyyppä, J., Hyyppä, H., & Kukko, A. (2008), Retrieval algorithms for road surface modelling using laser-based mobile mapping, *Sensors*, **8**(9), 5238–49.

Kukko, A., Andrei, C., Salminen, V., Kaartinen, H., Chen, Y., Rönnholm, P., Hyyppä, H., Hyyppä, J., Chen, R, Haggrén, H., Kosonen, I. & Capek, K. (2007), Road environment mapping system of the Finnish Geodetic Institute–Fgi Roamer, *International Archives of Photogrammetry,*

Remote Sensing and Spatial Information Sciences, **36**(3/W52), 241–7.
Lee, H. M. & Park, H. S. (2011), Gage-free stress estimation of a beam-like structure based on terrestrial laser scanning. *Computer-Aided Civil and Infrastructure Engineering*, **26**, 647–58.
Li, Q., Yao, M., Yao, X. & Xu, B. (2010), A real-time 3d scanning system for pavement distortion inspection, *Measurement Science and Technology*, **21**, 015702.
MRPT (2012), Mobile Robot Programming Toolkit webpage. Available at: http://mrpt.org/Rawlog-Format, accessed January 5, 2013.
NIMA (2000), *Department of Defense World Geodetic System of 1984. Its Definition and Relationships with Local Geodetic systems*, Technical Report 8350.2.
Nishikawa, T., Yoshida, J., Sugiyama, T. & Fujino, Y. (2012), Concrete crack detection by multiple sequential image filtering, *Computer-Aided Civil and Infrastructure Engineering*, **27**, 29–47.
Park, H. S., Lee, H. M., Adeli, H. & Lee, I. (2007), A new approach for health monitoring of structures: terrestrial laser scanning, *Computer-Aided Civil and Infrastructure Engineering*, **22**, 19–30.
Sareen, K. K., Knopf, G. K. & Canas, R. (2012), Consistent point clouds of narrow spaces using multiscan domain mapping, *Computer-Aided Civil and Infrastructure Engineering*, **27**, 555–72.
Shi, Y., Shibasaki, R. & Shi, Z. (2008), Towards automatic road mapping by fusing vehicle-borne multi-sensor data, *International Archives of the Photogrammetry, Remote Sensing and Spatial Information Sciences*, **37**, 867–72.
Shoemake, K. (1985), Animating rotation with quaternion curves, *ACM SIGGRAPH Computer Graphics*, **19**(3), 245–54.
SICK (2010), SICK Sensor Intelligence webpage. Available at: https://www.mysick.com/partnerPortal/ProductCatalog/DataSheet.aspx?ProductID=33769, accessed January 5, 2013.
Slob, S. & Hack, R. (2004), 3d terrestrial laser scanning as a new field measurement and monitoring technique, in *Engineering Geology for Infrastructure Planning in Europe*, p. 179–89.
Topcon (2012a), TOPCON Corporation webpage. Available at: http://www.topcon-positioning.eu/35/68/products.html, accessed January 5, 2013.
Topcon (2012b), TOPCON Corporation webpage. Available at: http://www.topconpositioning.com/legacy/gr-3, accessed January 5, 2013.
Topcon (2012c), TOPCON Corporation webpage. Available at: http://www.topconpositioning.com/products/machine-control/3d/3d-millimeter-gps, accessed January 5, 2013.
UMA (2011), University of Malaga webpage. Available at: http://www.uma.es/tnc/streaming/uma/RoadBot.html, accessed January 5, 2013.
Yu, S., Sukumar, S., Koschan, A., Page, D. & Abidi, M. (2007), 3d reconstruction of road surfaces using an integrated multisensory approach, *Optics and Lasers in Engineering*, **45**(7), 808–18.
Zalama, E., Gómez-García-Bermejo, J., Llamas, J. & Medina, R. (2011), An effective texture mapping approach for 3D models obtained from laser scanner data to building documentation, *Computer-Aided Civil and Infrastructure Engineering*, **26**, 381–92.
Zhang, C. & Elaksher, A. (2012), An unmanned aerial vehicle-based imaging system for 3D measurement of unpaved road surface distresses, *Computer-Aided Civil and Infrastructure Engineering*, **27**, 118–29.

APPENDIX A: ANALYTICAL ANALYSIS OF ERRORS IN HEIGHT

Here we present a theoretical derivation about the influence of the positioning system errors in the estimation of the surveyed points' height. In this derivation we will assume a perfect calibration of the laser scanner, hence not introducing any further error.

By combining Equations (12) and (13) we can work out the expression that relates the coordinates of a certain point on the ground with respect to the laser scanner's reference system and the coordinates of a point with respect to the global reference system, that is, the final coordinates of a surveyed point:

$$\mathbf{P}_i^E = \left[x_i^{\mathrm{E}}, y_i^{\mathrm{E}}, z_i^{\mathrm{E}}\right]^{\mathrm{T}} = \mathbf{T}_{\mathbf{V}}^{\mathbf{E}}\mathbf{T}_{\mathbf{S}}^{\mathbf{V}}\mathbf{P}_i^{\mathrm{S}} \tag{A.1}$$

For simplicity, we consider $\mathbf{T}_{\mathbf{S}}^{\mathbf{V}}$ (the homogeneous transformation matrix correspondent to the laser scanner's pose on the vehicle) to be the 4×4 identity matrix, because we assume here that calibration does not introduce any inaccuracies.

Thus, in Equation (A.1), the z coordinate (z_i^{E}) of the surveyed point follows the expression:

$$z_i^E = z_{LS} - r_i \sin(\beta)\cos(\alpha_i) + r_i \cos(\beta)\sin(\gamma)\sin(\alpha_i) \tag{A.2}$$

where z_{LS}, β, and γ stand for the z coordinate, *pitch,* and *roll* angles of the laser scanner, respectively, and r_i and α_i are the distance and angle of the point measured by the laser scanner, respectively.

Assuming a zero-mean, i.i.d. Gaussian distribution of the errors in height for the scanned point, its variance is computed as:

$$\sigma_{z_i^E}^2 = \mathbf{J} \cdot \mathrm{diag}\left(\sigma_\beta^2, \sigma_\gamma^2, \sigma_{z_{LS}}^2, \sigma_{r_i}^2, \sigma_{\alpha_i}^2\right) \cdot \mathbf{J}^{\mathrm{T}} \tag{A.3}$$

where $\mathbf{J}$ is the Jacobian vector of z_i^E with respect to the β, γ, z_{LS}, r_i, and α_i variables and the diagonal matrix contains the variances of those variables. This yields the following result:

$$\begin{aligned}\sigma_{z_i^E}^2 = {} & \sigma_{z_{LS}}^2 + \sigma_\beta^2(r_i \cdot \cos(\beta)\cos(\alpha_i) \\ & + r_i \cdot \sin(\beta)\sin(\gamma)\sin(\alpha_i))^2 \\ & + \sigma_{\alpha_i}^2(r_i \cdot \sin(\beta)\sin(\alpha_i) + r_i \cdot \cos(\beta)\sin(\gamma)\cos(\alpha_i))^2 \\ & + \sigma_{r_i}^2(\sin(\beta)\cos(\alpha_i) - \cos(\beta)\sin(\gamma)\sin(\alpha_i))^2 \\ & + \sigma_\gamma^2\left(r_i \cdot \cos(\beta)\cos(\gamma)\sin(\alpha_i)\right)^2\end{aligned} \tag{A.4}$$

Note that the error in the z coordinate of the laser scanner is purely cumulative to the final error, and that of the distance measurement is maximum when the scanning angle is zero. The rest of the errors depend on the measured range and the involved angles.

Finally, to consider only the effects of the inaccuracies related to the height estimation of the laser scanner and its error for the measured distance, we assume that the laser sensor orientation has been perfectly calibrated, and there is not uncertainty in its scanning angle, that is, $\sigma_\beta = \sigma_\gamma = \sigma_{\alpha i} = 0$. Then, by using the values for the pitch and roll angles shown in Table 1 and the standard deviations of the errors in both the distance measured by the laser scanner ($\sigma_{ri} = 10$ mm) and the height estimation of the positioning system ($\sigma_{zLS} = 6$ mm), equation results in a standard deviation of the errors in height of a surveyed point just under the vehicle ($\alpha_i = 0$) of about 11.86 mm, which approximately matches the presented results.

APPENDIX B: CLOSED-FORM SOLUTION FOR A POSE TRANSFORMATION

In this appendix we present an overview of the closed-form solution that computes the pose transformation

$$\tau_A^B = \langle \Delta x, \Delta y, \Delta z, \Delta\alpha, \Delta\beta, \Delta\gamma \rangle$$

between the B reference system with respect to the A reference system, given the coordinates of a set of N 3D points in both systems, $\{\mathbf{X}_A^i\}$ and $\{\mathbf{X}_B^i\}$.

This method can be summarized as follows:

1. Compute the centroids ($\mathbf{c}_A$ and $\mathbf{c}_B$) of the two sets of points and subtract them from their coordinates to deal only with coordinates relative to their centroids:

$$\begin{aligned} lll\mathbf{c}_A &= \frac{1}{N}\sum_{i=1}^{N}\mathbf{X}_A^i \\ \mathbf{c}_B &= \frac{1}{N}\sum_{i=1}^{N}\mathbf{X}_B^i \\ \overline{\mathbf{X}}_A^i &= \left(\bar{X}_A^i, \bar{Y}_A^i, \bar{Z}_A^i\right)^{\mathrm{T}} = \mathbf{X}_A^i - \mathbf{c}_A \\ \overline{\mathbf{X}}_B^i &= \left(\bar{X}_B^i, \bar{Y}_B^i, \bar{Z}_B^i\right)^{\mathrm{T}} = \mathbf{X}_B^i - \mathbf{c}_B \end{aligned} \tag{A.5}$$

2. For the i-th 3D point, compute the following nine products of its coordinates in both reference systems:

$$\begin{aligned} P_{XX}^i &= \bar{X}_A^i\bar{X}_B^i \quad P_{YX}^i = \bar{Y}_A^i\bar{X}_B^i \\ P_{XY}^i &= \bar{X}_A^i\bar{Y}_B^i \quad P_{YY}^i = \bar{Y}_A^i\bar{Y}_B^i \\ P_{XZ}^i &= \bar{X}_A^i\bar{Z}_B^i \quad P_{YZ}^i = \bar{Y}_A^i\bar{Z}_B^i \\ P_{ZX}^i &= \bar{Z}_A^i\bar{X}_B^i \quad P_{ZY}^i = \bar{Z}_A^i\bar{Y}_B^i \\ P_{ZZ}^i &= \bar{Z}_A^i\bar{Z}_B^i \end{aligned} \tag{A.6}$$

3. Accumulate the products in Equation (A.6) for all the 3D points to end up with the following nine values:

$$\begin{aligned} S_{XX} &= \sum_i P_{XX}^i \quad S_{YX} = \sum_i P_{YX}^i \\ S_{XY} &= \sum_i P_{XY}^i \quad S_{YY} = \sum_i P_{YY}^i \\ S_{XZ} &= \sum_i P_{XZ}^i \quad S_{YZ} = \sum_i P_{YZ}^i \\ S_{ZX} &= \sum_i P_{ZX}^i \quad S_{ZY} = \sum_i P_{ZY}^i \\ S_{ZZ} &= \sum_i P_{ZZ}^i \end{aligned} \tag{A.7}$$

4. Form a 4×4 symmetric matrix with the elements in Equation (A.7):

$$\mathbf{N} = \begin{pmatrix} N_{11} & N_{12} & N_{13} & N_{14} \\ N_{21} & N_{22} & N_{23} & N_{24} \\ N_{31} & N_{32} & N_{33} & N_{34} \\ N_{41} & N_{42} & N_{43} & N_{44} \end{pmatrix} \tag{A.8}$$

where

$$\begin{aligned} N_{11} &= S_{XX} + S_{YY} + S_{ZZ} \\ N_{12} &= N_{21} = S_{YZ} - S_{ZY} \\ N_{13} &= N_{31} = S_{ZX} - S_{XZ} \\ N_{14} &= N_{41} = S_{XY} - S_{YX} \\ N_{22} &= S_{XX} - S_{YY} - S_{ZZ} \\ N_{23} &= N_{32} = S_{XY} + S_{YX} \\ N_{24} &= N_{42} = S_{ZX} + S_{XZ} \\ N_{33} &= -S_{XX} + S_{YY} - S_{ZZ} \\ N_{34} &= N_{43} = S_{YZ} + S_{ZY} \\ N_{44} &= -S_{XX} - S_{YY} + S_{ZZ} \end{aligned} \tag{A.9}$$

5. Find the eigenvector corresponding to the largest eigenvalue of $\mathbf{N}$, which will be the quaternion that

determines the optimal rotation between the two sets of points.

6. Compute the rotation matrix ($\mathbf{R}$) associated to the so-obtained quaternion, and compute the translation $\mathbf{t} = (\Delta x, \Delta y, \Delta z)^T$ as the difference between the centroid at time in A and in B:

$$\mathbf{t} = \mathbf{c}_A - \mathbf{R}\mathbf{c}_B$$

7. Finally, we extract the values of the increments in *yaw*, *pitch*, and *roll* angles $\langle \Delta\alpha, \Delta\beta, \Delta\gamma \rangle$ between poses from the rotation matrix $\mathbf{R}$, having in this way all the components of τ_A^B.